IEEE Robotics and Automation Letters (RA-L) paper, presented at ICRA 2026, Vienna, Austria. Cite as RA-L paper.

Smooth and Robust Trajectory Tracking of Single-Actuator Monocopters via Incremental Nonlinear Dynamic Inversion

Emmanuel Tang, *Graduate Student Member, IEEE*, Xinyu Cai, Shawndy Michael Lee, and Shaohui Foong, *Member, IEEE*

***Abstract*—This letter presents a comprehensive comparative study of Incremental Nonlinear Dynamic Inversion (INDI) and standard Nonlinear Dynamic Inversion (NDI) for smooth trajectory tracking on Samara Seed-Inspired Single-Actuator Monocopters (SAM). While prior work on SAMs has largely focused on hover stabilization, smooth robust control for aggressive translational motion remains a largely uncharted frontier. Leveraging the precession-prone dynamics inherent to the SAM, we analyze the tracking performance of INDI across varying flight speeds, trajectories, and wing morphologies (long, short, ultralight). Our experiment results demonstrate that INDI on the long-wing consistently achieves lower angular acceleration tracking errors, reducing mean and RMS by up to 13.8% and 13.0%, respectively, while also improving motor efficiency with up to 8.4% less PWM usage compared to NDI. Additionally, INDI produces tighter and more stable body yaw rates ($\pm$ 0.1 Hz) and delivers up to 65% improvement in position tracking over traditional purely attitude control (ATT). Finally, even under severe actuation constraints with an ultralight-wing operating at reduced thrust, INDI maintains robust performance, validating its resistance towards precession and robust control of highly under-actuated SAMs.**

***Index Terms*—Biologically-inspired robots, sensor-based control, robust/adaptive control.**

I. Introduction

SAMARA Seed-Inspired Single-Actuator Monocopters (SAM) exhibit mechanical simplicity and flight endurance [1] for micro-aerial applications. Still, their continuous rotation induces strong precession and gyroscopic coupling that cannot be directly countered by external control surfaces or extra rotors, making aggressive trajectories exceedingly difficult to execute. Current methods to control the SAM—from positional PID [2] to purely attitude control (ATT) [3]—either assume simplistic dynamics or rely on limited feedback, which results in poor disturbance rejection, sensitivity to inertial mismatches, and large tracking errors on high-curvature paths. In this letter, we successfully apply Incremental Nonlinear Dynamic Inversion (INDI), which is resistant to precession and incrementally compensates for unmodeled dynamics, to the SAM using real-time angular-acceleration measurements with references generated via differential flatness.

A. Related Work

Incremental Nonlinear Dynamic Inversion (INDI) is popular as an advanced and robust sensor-reliant control technique for handling nonlinear systems [4], [5], [6], [7], [8], [9]. Improving from Nonlinear Dynamic Inversion (NDI) [10], a form of feedback linearization [11], INDI serves as a linear control strategy that updates the desired inputs incrementally using sensing feedback. Through the experiments done in [4], [12], [13], this method has proven robust for quadcopters, overcoming the inversion setbacks due to model fidelity as shown in early implementations of feedback linearization on rotorcraft [14]. Similarly, the foundation for Monocopters (first started with multiple actuators) was laid by [15], [16] with the platform a proof of concept, eventually progressing to aerial robots with utility [17]. As the design evolution of this platform ensued, the SAM was realized and flown/controlled with just one actuator via motor pulsing [2], suitable for applications that needed to fly for long [1], be lightweight, and low-cost. Further development in the use of attitude control (ATT) for the SAM was then evaluated in [3], where it demonstrated limited ability to follow only simple trajectories at low tracking speeds. In recent times, [18] adapted the Monocopter's dynamics for differential flatness [19] and showed its potential with aggressive trajectories with a variant platform [20]. To date, the collection of these works establishes the mechanical feasibility of SAM yet leaves open the challenge of achieving robust control on smooth and aggressive flight paths.

B. Contributions

Given the premise, this letter provides the following contributions to enhance smooth trajectory tracking for SAMs:

1) Novel application of INDI to the SAM, as shown in Fig. 1 with real-time motion capture validation, and benchmarking against NDI and ATT to quantify the practical benefits of incremental compensation.
2) Comprehensive comparison using different SAMs (long, short, ultralight-wings) quantifying control performance regarding angular-acceleration error, body yaw rates, motor effort, and 3D trajectory conformance.

Received 7 May 2025; accepted 13 September 2025. Date of publication 1 October 2025; date of current version 13 October 2025. This article was recommended for publication by Associate Editor S. Sun and Editor G. Loianno upon evaluation of the reviewers' comments. This work was supported by Temasek Laboratories @ SUTD and the Ministry of Education, Singapore under Grant T2EP50123-0017/MOE-T2EP50123-0004. *(Corresponding author: Shaohui Foong.)*

The authors are with the Engineering Product Development (EPD) Pillar, Singapore University of Technology and Design (SUTD), Singapore 487372 Singapore (e-mail: foongshaohui@sutd.edu.sg).

This article has supplementary downloadable material available at https://doi.org/10.1109/LRA.2025.3616650, provided by the authors.

Digital Object Identifier 10.1109/LRA.2025.3616650

IEEE Robotics and Automation Letters (RA-L) paper, presented at ICRA 2026, Vienna, Austria. Cite as RA-L paper.

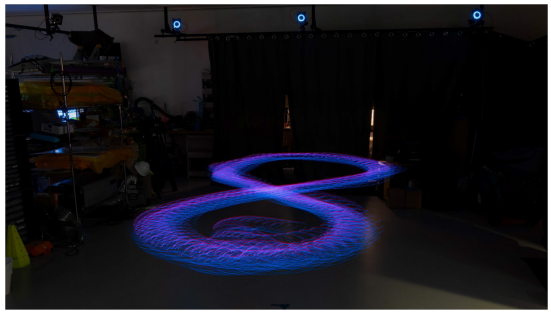

Fig. 1. SAM tracking a lemniscate continuously at an average speed of ~ 0.7 m/s.

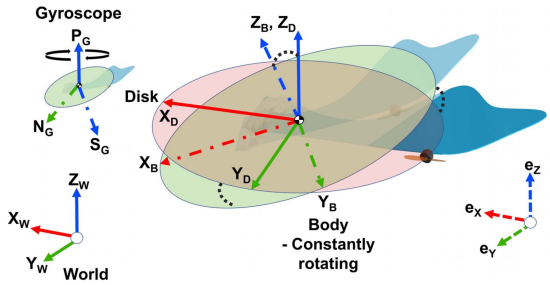

Fig. 2. Complete set of reference frames utilized for the Monocopter.

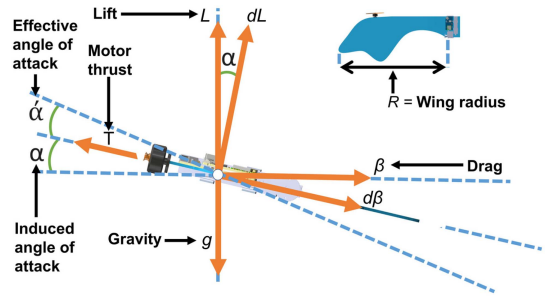

Fig. 3. SAM's side profile.

3) Empirical demonstration of INDI's resistance against precession and across varying inertia and thrust margins in the respective wings.

II. System Modeling

A. Notation

The SAM's various frames of reference in Fig. 2 are of the East-North-Up (ENU) basis, and consist of the world/inertia, body (observed during rotation), disk (observed during translation), and gyroscopic (observed during precession). The terminology used in this letter for equations and diagrams is summarized in Table I.

B. Modeling

1) Aerodynamic Forces: The SAM's aerodynamic lift force to sustain flight is denoted as L, and the force resisting its rotation is denoted β (see Fig. 3). Numerically, these terms are derived across the wing radius R using Blade Element Theory (see (1) and (2), symbols referenced in Table I)—used widely in helicopter aerodynamics [21].

$$dL = \frac{1}{2} C_L \rho c (\dot{\psi_B} r)^2 \mathrm{d}r, \quad d\beta = \frac{1}{2} C_\beta \rho c (\dot{\psi_B} r)^2 \mathrm{d}r \tag{1}$$

TABLE I
Nomenclature

Symbol	Description
$\{\mathbf{X_W}, \mathbf{Y_W}, \mathbf{Z_W}\} \in \mathbb{R}^3$	World-ENU basis.
$\{\mathbf{X_B}, \mathbf{Y_B}, \mathbf{Z_B}\} \in \mathbb{R}^3$	Body-ENU basis.
$\{\mathbf{X_D}, \mathbf{Y_D}, \mathbf{Z_D}\} \in \mathbb{R}^3$	Disk-ENU basis.
$\{\mathbf{P_G}, \mathbf{N_G}, \mathbf{S_G}\} \in \mathbb{R}^3$	Gyro-frame axes: precession, nutation, spin.
$\mathbf{Ref}, \mathbf{M}, \mathbf{Des}, \mathbf{C}, \mathbf{E}, \mathbf{Ext}$	(Reference, measured, desired, commanded, error, external) in subscript.
$\{\mathbf{P}, \mathbf{V}, \mathbf{A}, \mathbf{J}, \mathbf{S}\} \in \mathbb{R}^3$	Position, velocity, acceleration, jerk, snap.
$\{P_x, P_y, P_z\}$	Position error vector, $\mathbf{P_E} \in \mathbb{R}^3$.
$\{\phi, \theta, \psi\}$	Euler angles-(roll, pitch, and yaw), (B, D) in subscript refer to body and disk frame
$\{\dot{p}_G, \dot{n}_G, \dot{s}_G\}$	Precession, nutation, spin.
$\{\mathbf{\Phi_B}, \mathbf{\Phi_D}\} \in \mathbb{R}^3$	Attitude represented by Euler angles.
$\{\boldsymbol{\omega}_\mathbf{B}, \boldsymbol{\omega}_\mathbf{D}\} \in \mathbb{R}^3$	Angular rates.
$\{\dot{\boldsymbol{\omega}}_\mathbf{B}, \dot{\boldsymbol{\omega}}_\mathbf{D}\} \in \mathbb{R}^3$	Angular acceleration.
$\{\mathbf{Q_B}, \mathbf{Q_D}\} \in \mathbb{R}^4$	Quaternion vector (body, disk).
$\{\mathbf{R_Q}, \mathbf{T_\Phi}\} \in \mathbb{R}^{3x3}$	Rotation, transformation matrix.
$\mathbf{y} \in \mathbb{R}^4$, k, Ts	Flat-outputs, timestep, sample time.
$\alpha/\acute{\alpha}, m, R$	Induced/effective angle of attack, mass, wing radius.
C_L, C_β, c, ρ	Coefficients of lift and drag, local blade chord, air density.
I_{xx}, I_{yy}, I_{zz}	Inertia tensor diagonal elements.
$\mathbf{I} \in \mathbb{R}^{2x2}$	Inertia square matrix (I_{xx}, I_{yy}).
$L, \beta, g, \mathrm{T}, \tau$	Lift / Collective input, drag, gravity, thrust, torque (e.g., τ_{X_D}, τ_{N_G} about $\mathbf{X_D}$ and $\mathbf{N_G}$).
$\odot, \times, \cdot, \zeta$	Quaternion-rotation, cross product, dot product, angle between vectors.
$M(s), H(s), \Delta\mathrm{f}$	(Motor, filter transfer functions), modeling error.
$\boldsymbol{\gamma}_\mathbf{TP} \in \mathbb{R}^{2x2}$, $\mu_\mathbf{TP}$	Control effectiveness and motor pulsing input.

$$L = \int_0^R (dL \cos(\alpha) - d\beta \sin(\alpha))$$
$$\beta = \int_0^R (dL \sin(\alpha) + d\beta \cos(\alpha)) \tag{2}$$

2) Reduced Combined Dynamics: Secondly, in modeling the disk/Tip Path Plane (TPP) similar to [18], ($\mathbf{X_D}$-$\mathbf{Y_D}$) as illustrated in Fig. 2 has its principal axes of inertia collinear with the $\mathbf{W}$ frame where ψ_D is always 0. This plane is linked to the annular motion [21] of the wing tips when the body is rotating, with its attitude $\mathbf{\Phi_D}$ and derivative $\dot{\mathbf{\Phi}}_\mathbf{D}$ tracked. The attitude rates are then transformed into disk angular rates $\boldsymbol{\omega_D}$ using the transformation matrix $\mathbf{T_\Phi}$ in (4). Lastly, the SAM functions like a rotating axisymmetric body, much like a gyroscope [18]. Therefore, the reduced combined dynamics, which account for the balance of both linear and angular momentum, can be described as follows in (3) and (5):

$$\dot{\mathbf{P}} = \mathbf{V}, \quad \dot{\mathbf{V}} = \left(\frac{L}{m}\right) \mathbf{Z_D} - g\mathbf{Z_W} \tag{3}$$

$$\boldsymbol{\omega_D} = \mathbf{T_\Phi} \cdot \dot{\mathbf{\Phi}}_\mathbf{D} \tag{4}$$

$$\dot{\boldsymbol{\omega}}_\mathbf{D} = \mathbf{I}^{-1}(\boldsymbol{\tau_D} - \boldsymbol{\omega_D} \times (\mathbf{I}\boldsymbol{\omega_D})) \tag{5}$$

For linear and angular momentum, the lift term L represents the collective thrust needed along the $\mathbf{Z_D}$ axis against gravity g of 9.81 m/s^2. I_{xx} and I_{yy} denote the principal moments of inertia about $\mathbf{X_D}$ and $\mathbf{Y_D}$ whilst I_{zz} denotes the moment of inertia about $\mathbf{Z_B}$.

3) Precession: Considering the collinearity of $\mathbf{N_G}$ with $\mathbf{X_D}$ and $\mathbf{Y_D}$ [18] in (6), the nutation torque τ_{N_G} combines the torque τ about $\mathbf{X_D}$ and $\mathbf{Y_D}$. Together with $\dot{\psi}_B$, the intrinsic dynamic

IEEE Robotics and Automation Letters (RA-L) paper, presented at ICRA 2026, Vienna, Austria. Cite as RA-L paper.

of precession $\dot{p}_G$ becomes prominent due to (7), and undesired as it disrupts tracking as shown in [2].

$$\because \mathbf{N_G} \times \mathbf{X_D} = 0 | \tau_{Y_D} = 0 \Rightarrow \mathbf{N_G} \times \mathbf{Y_D} = 0 | \tau_{X_D} = 0 \quad (6)$$

$$\left\{ \dot{p}_G = \frac{\tau_{N_G}}{I_{zz}\dot{\psi}_B} \right\} : \{ \tau_{N_G} = \tau_{X_D} + \tau_{Y_D} \}$$

$$\text{s.t.} \quad \{ \dot{\psi}_B = \dot{s}_G, \quad I_{xx} = I_{yy} \} \quad (7)$$

C. Differential Flatness

For a differentially flat system like the Monocopter as a disk analyzed in [18], there exist algebraic functions of a set of four flat outputs $\{\mathbf{y} = [\mathbf{P_{Ref}}, \psi_{\mathbf{Ref}}]^T : \mathbf{P_{Ref}} \in \mathbb{R}^3\}$ and a limited number of their time derivatives [19]-(generated via calculus of variations) to find feedforward references for angular rates and acceleration.

1) Orientation of the Disk: To begin, an intermediary orthonormal basis made up of unit vectors $\{e_x, e_y, e_z\}$ in Fig. 2 is used. This basis aligns with the disk axes $\mathbf{X_D}$ and $\mathbf{Y_D}$ when it is projected onto the world plane $\mathbf{X_W}$-$\mathbf{Y_W}$. To then compute the orientation of the disk, we apply an arbitrary desired linear acceleration vector $\mathbf{A_{Des}} \in \mathbb{R}^3$ into the following expression that attains $\mathbf{X_D}$ and $\mathbf{Y_D}$ as the unit vector of the cross product of $\mathbf{A_{Des}}$ and the intermediary basis vectors as outlined in [22]:

$$\mathbf{Y_D} = \frac{\mathbf{A_{Des}} \times \mathbf{e_x}}{\|\mathbf{A_{Des}} \times \mathbf{e_x}\|_2}, \quad \mathbf{X_D} = \frac{\mathbf{e_y} \times \mathbf{A_{Des}}}{\|\mathbf{e_y} \times \mathbf{A_{Des}}\|_2}, \quad \psi_{\mathbf{D}} = \mathbf{0} \quad (8)$$

2) Collective Thrust L and Body Yaw Rate $\dot{\psi}_B$: From (2), L and $\dot{\psi}_B$ is determined from linearisation via the following small-angle approximations:

$$\mathbf{Z_D^T}(\mathbf{A_{Des}}) = \left(\frac{L}{m}\right) \quad | \quad \cos(\alpha) \approx 1, \sin(\alpha) \approx 0 \quad (9)$$

3) Jerk Tracking Via Angular Rates of the Disk $\boldsymbol{\omega}_{\mathbf{D_{Ref}}}$: Taking reference and differentiating from (3), jerk $\mathbf{J_{Ref}}$ is referenced from the flat outputs to solve for the reference rates as outlined in [22]:

$$\mathbf{J_{Ref}} = \dot{\mathbf{A}}_{\mathbf{Ref}}, \quad \mathbf{J_{Ref}} = \left(\frac{L}{m}\right)(\dot{\phi}_D \mathbf{X_D} - \dot{\theta}_D \mathbf{Y_D}) + \left(\frac{\dot{L}}{m}\right)\mathbf{Z_D} \quad (10)$$

And using the properties in forming an orthonormal basis, the rates can therefore be:

$$\dot{\phi}_{D_{\mathbf{Ref}}} = \frac{\mathbf{X_D}^T \cdot \mathbf{J_{Ref}}}{(\frac{L}{m})}, \quad \dot{\theta}_{D_{\mathbf{Ref}}} = \frac{\mathbf{Y_D}^T \cdot \mathbf{J_{Ref}}}{(-\frac{L}{m})} \quad (11)$$

The values for $\dot{\psi}_{D_{\mathbf{Ref}}}$ and $\ddot{\psi}_{D_{\mathbf{Ref}}}$ are null as yaw control is not required for the disk.

4) Snap Tracking Via Angular Acceleration of the Disk $\dot{\boldsymbol{\omega}}_{\mathbf{D_{Ref}}}$: Finally, to compute the disk's reference angular acceleration and torque inputs based on the flat outputs, snap $\mathbf{S_{Ref}}$ is referenced using the exact mathematical manipulation performed in (10) and (11), leading to the following expression:

$$\ddot{\phi}_{D_{\mathbf{Ref}}} = \frac{\mathbf{X_D}^T \cdot \mathbf{S_{Ref}}}{(\frac{L}{m})}, \quad \ddot{\theta}_{D_{\mathbf{Ref}}} = \frac{\mathbf{Y_D}^T \cdot \mathbf{S_{Ref}}}{(-\frac{L}{m})} \quad | \quad \mathbf{S_{Ref}} = \dot{\mathbf{J}}_{\mathbf{Ref}} \quad (12)$$

III. Control Strategy Overview

1) $\mathbf{X_W}$-$\mathbf{Y_W}$ Horizontal Translation: Fig. 4 shows a high-level overview of the cascaded controller (including feedforward terms) with in-depth schematics in Fig. 5. From the desired angular acceleration block onward, the inputs are incrementally computed to compensate for unmodeled dynamics and disturbances. These signals are then mapped to motor commands

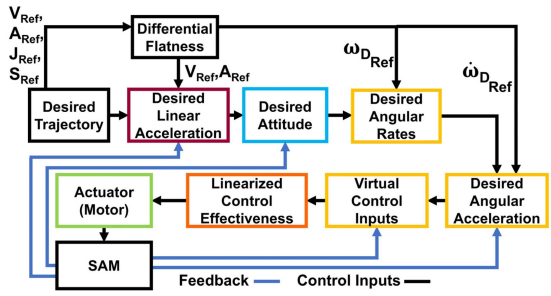

Fig. 4. Block diagram of the entire cascaded controller.

through the linearized control effectiveness block tailored to the SAM's flight response. Coupled with real-time full state feedback, these laws provide robust horizontal control of the SAM against the offset of precession.

2) $\mathbf{Z_W}$ Vertical Translation (Collective): To achieve smooth tracking along $\mathbf{Z_W}$, the control law used is (9), referencing the desired acceleration via (13).

B. Desired Linear Acceleration

The cascaded control framework first computes the desired linear acceleration vector $\mathbf{A_{Des}} \in \mathbb{R}^3$, as introduced in Section II-C. Via (13), $\mathbf{A_{Des}}$ is computed using position, referenced velocity, and feedback, along with referenced acceleration fed forward from the flat outputs. This is supplemented with positive definite gain matrices of $\{\text{Kp}, \text{Ki}, \text{Kv}\} \in \mathbb{R}^{3\text{x}3}$.

$$\mathbf{A_{Des}} = \text{Kp}(\mathbf{P_E}) + \text{Ki}\left(\int_0^{\text{Ts}} \mathbf{P_E dt}\right) + \text{Kv}(\mathbf{V_E}) + \mathbf{A_{Ref}} - g\mathbf{Z_W} \mid \mathbf{P_E} = \mathbf{P_{Ref}} - \mathbf{P_M}, \mathbf{V_E} = \mathbf{V_{Ref}} - \mathbf{V_M} \quad (13)$$

C. Desired Attitude (ATT)

This section (as highlighted in cyan in Fig. 5) encompasses the following expressions to find the error quaternion $\mathbf{Q_{D_E}} \in \mathbb{R}^4$, using the globally asymptotically stable control law fully derived in [23]. Attitude control (ATT) was used in [3] and [18] as the main method as well:

$$\mathbf{Q_{D_E}} = \left[\cos(\zeta/2) \quad \left(\mathbf{Q_{D_M}^{-1}} \odot \frac{\hat{\mathbf{Z}}_\mathbf{D} \times \hat{\mathbf{A}}_\mathbf{Des}}{\|\hat{\mathbf{Z}}_\mathbf{D} \times \hat{\mathbf{A}}_\mathbf{Des}\|_2}\right) \sin(\zeta/2)\right]^\mathbf{T}.$$

$$| \hat{\mathbf{Z}}_\mathbf{D} = \mathbf{Q_{D_M}} \odot \mathbf{Z_D}, \hat{\mathbf{A}}_\mathbf{Des} = \frac{\mathbf{A_{Des}}}{\|\mathbf{A_{Des}}\|_2}, \zeta = \arccos(\hat{\mathbf{Z}}_\mathbf{D} \cdot \hat{\mathbf{A}}_\mathbf{Des}) \quad (14)$$

$$\mathbf{\Phi_{D_{Des}}} = \text{K}_\Phi \cdot \begin{bmatrix} \phi_{D_\mathbf{E}} & \theta_{D_\mathbf{E}} \end{bmatrix}^T = \text{K}_\Phi \cdot \begin{bmatrix} \mathbf{Q_{D_E}}_{2,1} & \mathbf{Q_{D_E}}_{1,1} \end{bmatrix}^T. \quad (15)$$

With a positive definite diagonal gain matrix of $\text{K}_\Phi \in \mathbb{R}^{2\text{x}2}$, and $\phi_{D_\mathbf{E}}$ and $\theta_{D_\mathbf{E}}$ extracted from $\mathbf{Q_{D_E}}$ in (14), a reduced $\mathbf{\Phi_{D_{Des}}} \in \mathbb{R}^2$ is attained via (15).

D. Desired Angular Rates With References

$$\boldsymbol{\omega}_{\mathbf{D_{Des}}} = \mathbf{\Phi_{D_{Des}}} + \boldsymbol{\omega}_{\mathbf{D_{Ref}}} \quad (16)$$

$\boldsymbol{\omega}_{\mathbf{D_{Des}}} \in \mathbb{R}^2$ is then attained in (16) with angular rate references $\boldsymbol{\omega}_{\mathbf{D_{Ref}}} \in \mathbb{R}^2$ from Section II-C3.

IEEE Robotics and Automation Letters (RA-L) paper, presented at ICRA 2026, Vienna, Austria. Cite as RA-L paper.

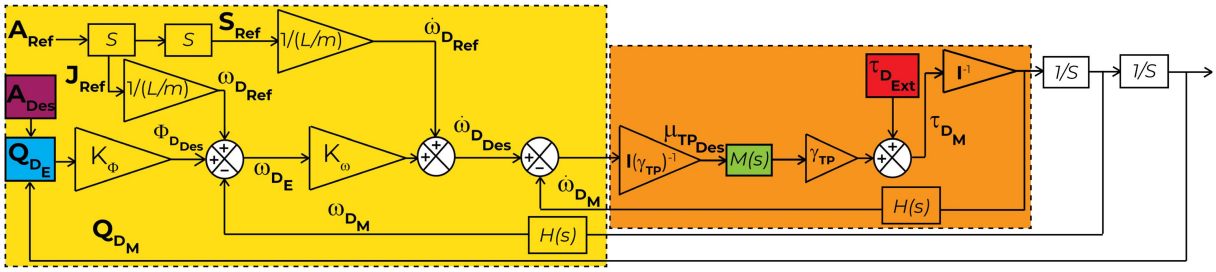

Fig. 5. Cascaded Control Framework for Horizontal Motion ($\mathbf{X_W}$-$\mathbf{Y_W}$ Translation at Constant Altitude) - Reference sections colored in III-B, III-C, III-D, III-E, III-F, III-G, IV, and IV (same section).

E. Desired Angular Acceleration With References

To find the reduced desired angular acceleration $\dot{\boldsymbol{\omega}}_{\mathbf{D_{Des}}} \in \mathbb{R}^2$, (17) is used with angular acceleration references $\dot{\boldsymbol{\omega}}_{\mathbf{D_{Ref}}} \in \mathbb{R}^2$ from Section II-C4, where $\mathrm{K}_\omega \in \mathbb{R}^{2x2}$ is a positive definite diagonal matrix with derivative gains:

$$\dot{\boldsymbol{\omega}}_{\mathbf{D_{Des}}} = \mathrm{K}_\omega \cdot (\boldsymbol{\omega}_{\mathbf{D_E}}) + \dot{\boldsymbol{\omega}}_{\mathbf{D_{Ref}}} \quad | \quad \boldsymbol{\omega}_{\mathbf{D_E}} = \boldsymbol{\omega}_{\mathbf{D_{Des}}} - \boldsymbol{\omega}_{\mathbf{D_M}} \tag{17}$$

F. Virtual Control Inputs

1) Nonlinear Dynamic Inversion: As shown in [8], Nonlinear Dynamic Inversion (NDI) performs pure model inversion in (5) and takes in full control input from $\dot{\boldsymbol{\omega}}_{\mathbf{D_{Des}}}$. Because $\dot{\psi}_{D_\mathbf{M}}$ is null given $\psi_{D_\mathbf{M}}$ is always 0, the nonlinear term in (5) becomes nullified. Hence, the NDI control law generates the desired disk torque as the commanded torque $\boldsymbol{\tau}_{\mathbf{D_C}} \in \mathbb{R}^2$:

$$\boldsymbol{\tau}_{\mathbf{D_C}} = \boldsymbol{\tau}_{\mathbf{D_{Des}}} = \mathbf{I} \cdot \dot{\boldsymbol{\omega}}_{\mathbf{D_{Des}}} \quad | \quad \mathbf{I} \in \mathbb{R}^{2x2} \tag{18}$$

2) Incremental Nonlinear Dynamic Inversion:: Incremental Nonlinear Dynamic Inversion (INDI), on the other hand, incrementally corrects toward the desired angular acceleration by relying on angular acceleration measurements, making it robust towards modeling errors [4]. Therefore, the INDI control law in incremental form generates the error in the disk torque as the commanded torque $\boldsymbol{\tau}_{\mathbf{D_C}} \in \mathbb{R}^2$:

$$\boldsymbol{\tau}_{\mathbf{D_C}} = \boldsymbol{\tau}_{\mathbf{D_{Des}}} - \boldsymbol{\tau}_{\mathbf{D_M}} = \mathbf{I} \cdot (\dot{\boldsymbol{\omega}}_{\mathbf{D_{Des}}} - \dot{\boldsymbol{\omega}}_{\mathbf{D_M}}) \quad | \quad \mathbf{I} \in \mathbb{R}^{2x2} \tag{19}$$

G. Linearized Control Effectiveness Inversion

In INDI/NDI control law, the controleffectiveness matrix $\boldsymbol{\gamma}_{\boldsymbol{\gamma}_{\mathbf{TP}}} \in \mathbb{R}^{2x2}$ directly maps the commanded/desired forces and torques into platformspecific lowlevel actuator commands [4] shown in the linearized expression in (20). Specifically for the SAM, using its native $\boldsymbol{\gamma}_{\boldsymbol{\gamma}_{\mathbf{TP}}}$, the desired motor pulses for horizontal motion $\boldsymbol{\mu}_{\mathbf{TP_{Des}}} \in \mathbb{R}^{1x2}$ [2] can be attained after the commanded torque is generated. As the SAM has only one actuator, the collective input L is added in (21) to compute a single commanded motor pulse $\mu_{\mathbf{TP_C}}$ to generate thrust, T:

$$\boldsymbol{\mu}_{\mathbf{TP_{Des}}} = {\boldsymbol{\tau}_{\mathbf{D_C}}}^T \cdot \boldsymbol{\gamma}_{\mathbf{TP}}^{-1} \tag{20}$$

$$\mu_{\mathbf{TP_C}} = \boldsymbol{\mu}_{\mathbf{TP_{Des}}1,1} + \boldsymbol{\mu}_{\mathbf{TP_{Des}}1,2} + L \tag{21}$$

IV. Simulated Disturbance Rejection

To validate the robustness of INDI as mentioned in Section III-F2 in handling modeling discrepancies on the SAM, an external step disturbance torque of 0.5 Nm was applied onto the innermost angular acceleration loop in Fig. 5 via numerical simulation in MATLAB using the transfer function in (22). The motor's transfer function $M(s)$ is that of the brushless-DC motor (ROBO 1303.5) mounted on the SAM, with values approximated from the manufacturer's specifications sheet. The low-pass filter's transfer function is denoted as $H(s)$, and Δf denotes the modeling error.

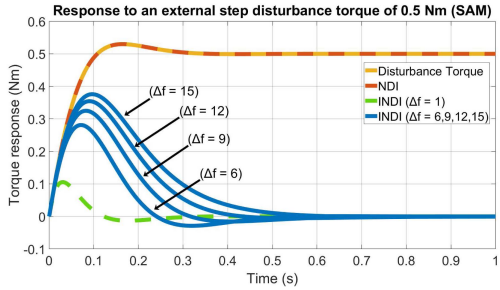

Fig. 6. Simulating disturbance rejection in the angular acceleration loop in Fig. 5 subject to varying modeling errors.

$$\frac{\boldsymbol{\tau}_{\mathbf{D_M}}}{\boldsymbol{\tau}_{\mathbf{D_{Ext}}}} = \frac{\Delta f}{\Delta f + H(s)M(s)} \tag{22}$$

Shown in Fig. 6, NDI relies heavily on an accurate system model, making it susceptible to external disturbances. INDI inherently compensates for these uncertainties by leveraging angular acceleration measurements. By directly observing how the system responds to control inputs and disturbances, INDI can apply corrections incrementally even with discrepancies in the model's fidelity.

V. Flight Experiments

This section presents the flight experiments conducted with three SAMs (sharing a similar design but differing in wingspans, weights, and actuators), aimed at testing and validating the tracking performance of NDI and INDI across various trajectories at different velocities.

A. SAM Electronics and Parts

The SAM design presented in this letter follows the approach of [3], with only three onboard electronic components involved in power supply and consumption: a 2S LiPo battery for power, a Crazyflie Bolt 1.1 running customized firmware to receive motor commands, and a brushless-DC motor paired with an electronic speed controller (ESC) for closed-loop voltage control, as illustrated in Fig. 7.

IEEE Robotics and Automation Letters (RA-L) paper, presented at ICRA 2026, Vienna, Austria. Cite as RA-L paper.

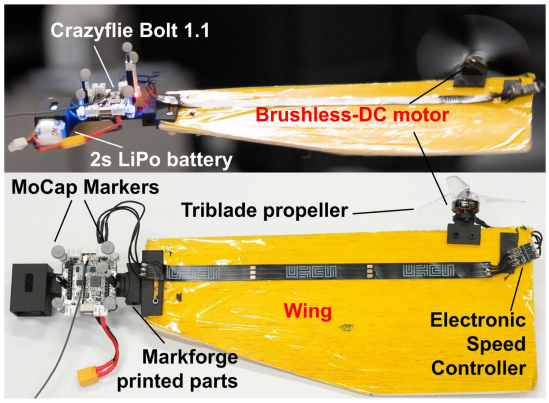

Fig. 7. Standardized Suite of Electronics across all wings.

TABLE II
COMPARISON OF SAM WINGS

SAM (wing)	Short	Long	Ultralight
Wingspan (cm)	23	34	31
Wing material	Balsa wood	Balsa wood	Foam
Wing thickness (mm)	2	1	1
Powered weight (g)	64	58	32
Battery cells in series	2	2	1
Brushless-DC motor	ROBO 1303.5	ROBO 1303.5	BR1103
Motor max thrust (g)	∼80–90	∼80–90	∼25–30
Thrust-To-Weight ratio	∼1.2–1.4x	∼1.2–1.4x	∼0.6–0.75x

Fig. 8. SAM wings from left to right: short, long, ultralight; respective gains from top to bottom: short, long, ultralight.

B. SAM Wings

Table II and Fig. 8 summarize and illustrate the differences among the three SAMs along with their respective gains, whilst Fig. 9 shows the yaw rate of each craft under INDI.

C. Discrete Time State Estimation in Environment

Flight experiments were conducted in an indoor flying arena measuring 4 m × 4 m, and equipped with an OptiTrack motion capture system, where the system fed position and orientation data at 250 Hz to an offboard computer, which runs the flight

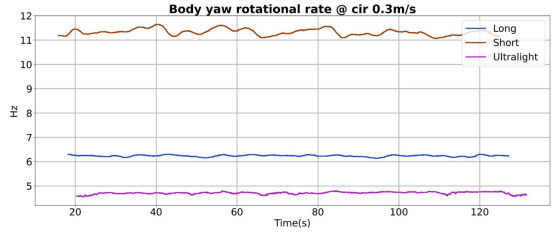

Fig. 9. Comparison in the Body Yaw Rotational Rate among the SAM wings when controlled via INDI.

controls at 250 Hz and transmits the motor commands to the Bolt via the Crazyradio dongle.

1) Attitude Estimation: To instantaneously estimate the disk/TPP's attitude in real-time, the vector $\mathbf{X_B}$ of the rotating body in Fig. 2 is referenced from the rotation matrix $\mathbf{R_Q}$ [24], which is computed from the quaternion vector of the rotating body $\mathbf{Q_{B_M}} = [\mathbf{Q_{B_{w_M}}} \quad \mathbf{Q_{B_{x_M}}} \quad \mathbf{Q_{B_{y_M}}} \quad \mathbf{Q_{B_{z_M}}}]^T$ to produce $\mathbf{\Phi_{D_M}}$.

$$\mathbf{X_B} = \begin{bmatrix} \mathbf{R_{Q_{1,1}}} \\ \mathbf{R_{Q_{2,1}}} \\ \mathbf{R_{Q_{3,1}}} \end{bmatrix} = \begin{bmatrix} 1 - 2(\mathbf{Q^2_{B_{y_M}}} + \mathbf{Q^2_{B_{z_M}}}) \\ 2(\mathbf{Q_{B_{x_M}}}\mathbf{Q_{B_{y_M}}} + \mathbf{Q_{B_{w_M}}}\mathbf{Q_{B_{z_M}}}) \\ 2(\mathbf{Q_{B_{x_M}}}\mathbf{Q_{B_{z_M}}} + \mathbf{Q_{B_{w_M}}}\mathbf{Q_{B_{y_M}}}) \end{bmatrix}. \tag{23}$$

$$\mathbf{\Phi_{D_M}} = \begin{bmatrix} -\sin(\psi_B)(\frac{\pi}{2} - \arccos(\mathbf{X_B}^T \cdot \mathbf{Z_D})) \\ \cos(\psi_B)(\frac{\pi}{2} - \arccos(\mathbf{X_B}^T \cdot \mathbf{Z_D})) \\ 0 \end{bmatrix}. \tag{24}$$

2) Attitude Derivatives: Due to the high rotational rate $\dot{\psi}_B$ of the SAMs exceeding the saturation limit of the onboard gyro at 5.56 Hz on the Bolt [25], the SAM's attitude derivatives, $\dot{\mathbf{\Phi}}_{\mathbf{D_M}}$ and $\ddot{\mathbf{\Phi}}_{\mathbf{D_M}}$, were approximated [26] using discrete central difference in (25) and (26) on $\mathbf{\Phi_{D_M}}$ obtained in Section V-C1 before eventually passing through a fifth-order butterworth filter with cutoff frequency of 30 Hz. This setup ensured reliable and accurate measurements before transforming into angular rates in (4), and acceleration in (27).

$$\dot{\mathbf{\Phi}}_{\mathbf{D_M}}\Big|_{k=1} \approx \frac{\mathbf{\Phi}_{\mathbf{D_M}\,k+1} - \mathbf{\Phi}_{\mathbf{D_M}\,k-1}}{2\mathrm{Ts}} \tag{25}$$

$$\ddot{\mathbf{\Phi}}_{\mathbf{D_M}}\Big|_{k=1} \approx \frac{\mathbf{\Phi}_{\mathbf{D_M}\,k+1} - 2\mathbf{\Phi}_{\mathbf{D_M}\,k} + \mathbf{\Phi}_{\mathbf{D_M}\,k-1}}{(\mathrm{Ts})^2} \tag{26}$$

$$\boldsymbol{\omega}_{\mathbf{D_M}} = \mathbf{T_\Phi} \cdot \ddot{\mathbf{\Phi}}_{\mathbf{D_M}} + \dot{\mathbf{T}}_{\mathbf{\Phi}} \cdot \dot{\mathbf{\Phi}}_{\mathbf{D_M}} \tag{27}$$

D. Control Effectiveness

Phase delay [21] occurs for most aerial systems relying on blades/wings rotating rapidly. As the phase delay for SAMs is revealed through physical flight tests (both manual and autonomous), it serves as the system's control effectiveness in ensuring the correct direction during horizontal motion. Eq (28) is an example of the control effectiveness of a wing that has a $\frac{\pi}{2}$ phase delay:

$$\boldsymbol{\gamma_{TP}} = \begin{bmatrix} -\cos(\psi_B) & 0 \\ 0 & -\sin(\psi_B) \end{bmatrix}^{-1}. \tag{28}$$

IEEE Robotics and Automation Letters (RA-L) paper, presented at ICRA 2026, Vienna, Austria. Cite as RA-L paper.

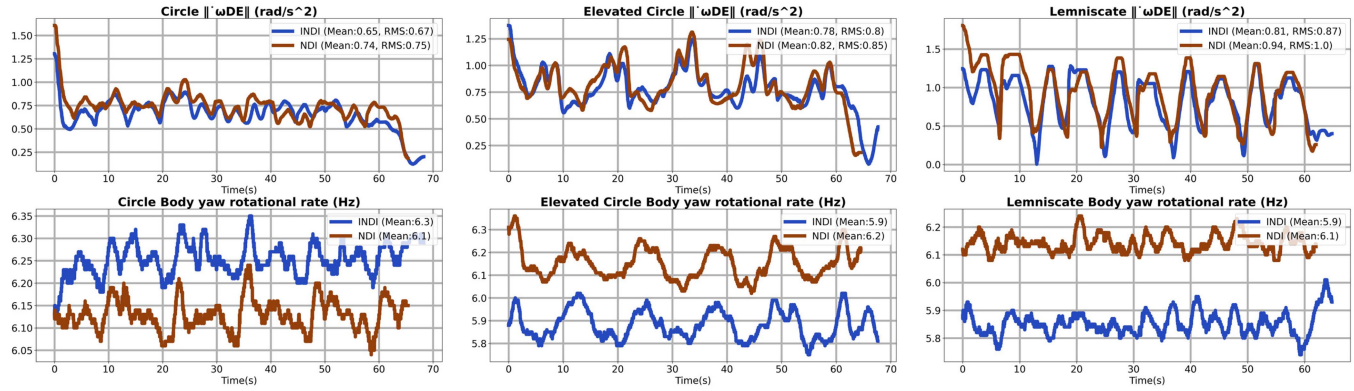

Fig. 10. Long-wing: angular acceleration error $\|\dot{\boldsymbol{\omega}}_{\mathbf{De}}\|_2$ (rad/s^2), and body yaw rotational rate (Hz).

TABLE III
REFERENCE TRAJECTORIES: NUMBER OF LAPS PER TRAJECTORY, N; AVERAGE AND PEAK VELOCITY (M/S) AND ACCELERATION (M/s^2) NORMS

Trajectory	$\|\overline{\mathbf{V}_{\mathbf{Ref}}}\|_2$	$\|\mathbf{V}_{\mathbf{Ref}_{\max}}\|_2$	$\|\overline{\mathbf{A}_{\mathbf{Ref}}}\|_2$	$\|\mathbf{A}_{\mathbf{Ref}_{\max}}\|_2$
Circle (N=5)	0.50	0.62	0.25	0.70
Elevated circle (N=5)	0.53	0.66	0.27	0.78
Lemniscate (N=5)	0.65	0.78	0.60	3.80

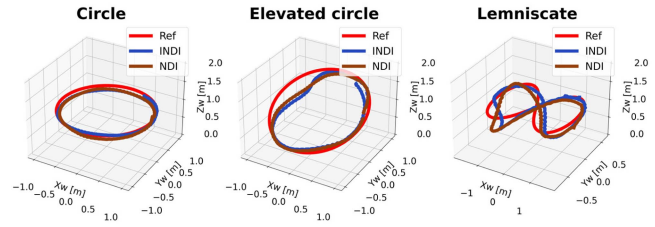

Fig. 11. Long-wing: 3D reference trajectories against the average lap flown by INDI and NDI.

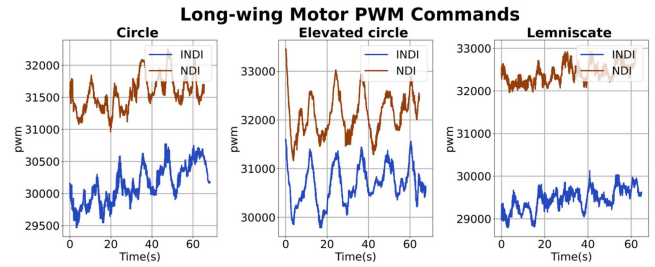

Fig. 12. Long-wing: motor PWM between INDI and NDI.

E. Experiment Results

The experiments were conducted in three phases to systematically evaluate the tracking performance of the controllers across different wings (long, short, ultralight). Table III can be referred to for the required laps, velocities, and acceleration, whilst Fig. 11 illustrates the geometrical boundaries of the reference trajectories.

TABLE IV
LONG-WING: MEAN OF NORM ERROR FOR EACH TRAJECTORY AND METHOD IN FIG. 10; % ERROR REDUCED OVER NDI

Trajectory	INDI (Mean ± σ)	NDI (Mean ± σ)	Δ Mean (%)[2]
Circle	0.65 ± 0.16	0.74 ± 0.12	–12.2
Elevated circle	0.78 ± 0.18	0.82 ± 0.22	–4.9
Lemniscate	0.81 ± 0.32	0.94 ± 0.34	–13.8

1) *Long-wing* (INDI vs. NDI) in Section V-F1: Direct comparison in angular acceleration error, motor PWM, and body yaw rate.
2) *Long-wing, Short-wing* (INDI vs. NDI vs. Purely Attitude Control (ATT)-(see Section III-C)) in Section V-F2: Analysis of position error, $\mathbf{P_E} = [Px \quad Py \quad Pz]^T$.
3) *Ultralight-wing* (INDI vs. NDI) in Section V-F3: Analysis of position error, $\mathbf{P_E} = [Px \quad Py \quad Pz]^T$, over a reduced number of trajectories and velocities.

F. Discussion

1) Long-Wing (INDI Vs. NDI): The experimental results decisively demonstrate INDI's superiority over NDI across all three core metrics: angular acceleration error tracking, motor actuation effort, and body yaw rate stability. As shown in Table IV,[1] INDI has a consistently lower $\|\dot{\boldsymbol{\omega}}_{\mathbf{De}}\|_2$ mean that's down by 13.8%, echoing the results in Fig. 6, and highlighting its ability to track rapid rotational dynamics better–particularly in precession prominent regimes like the lemniscate. Simultaneously, INDI exhibits better motor efficiency by reducing PWM commands by 4.4–8.4% across all trajectories (Table V),[2] as shown in Fig. 12 and reflecting less aggressive and more refined control effort to achieve better trajectory tracking. Furthermore, INDI yields more stable and slightly lower body yaw rotational rates, maintaining deviations within ±0.1 Hz, as opposed to ±0.15 Hz under NDI (Table V(b)). This tighter spread demonstrates a smoother control loop and enhanced precession resistance. These findings highlight INDI's ability to deliver more accurate, efficient, and stable tracking performance compared to NDI, as shown in the average lap traversed in Fig. 11.

[1] %Values in green mean a reduction, whilst red indicates an increase
[2] B. Sensortec, "Bmi088 - data sheet." Online, Apr. 2020. Rev. 1.6.

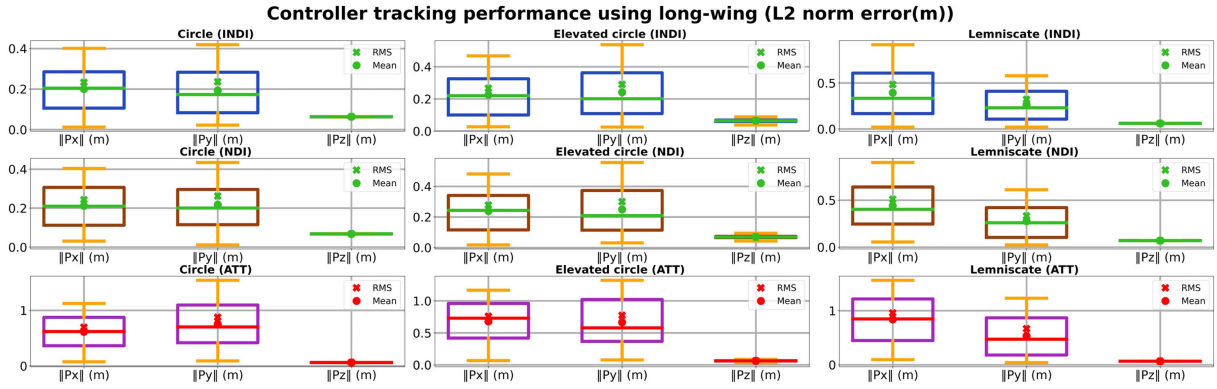

Fig. 13. Long-wing: controller position tracking performance for $\|Px\|_2$, $\|Py\|_2$, $\|Pz\|_2$.

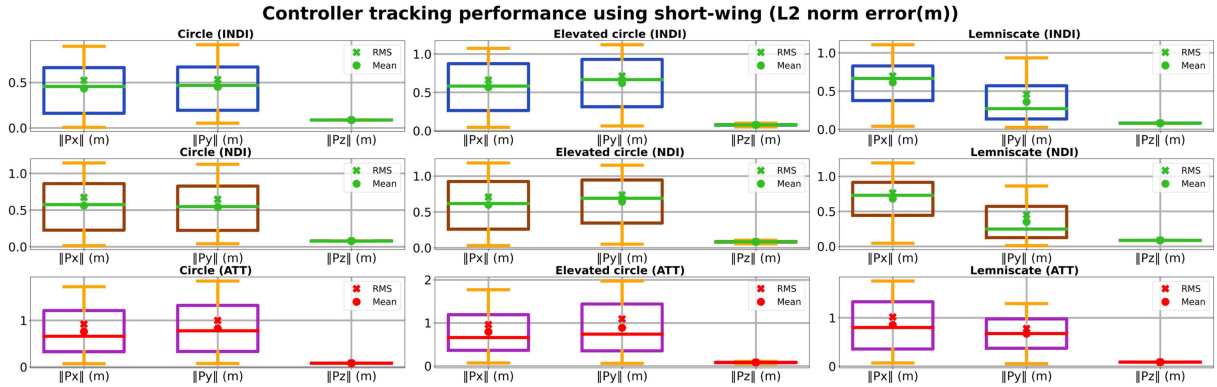

Fig. 14. Short-wing: controller position tracking performance for $\|Px\|_2$, $\|Py\|_2$, $\|Pz\|_2$.

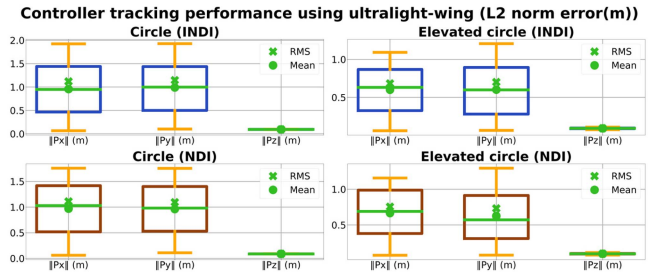

Fig. 15. Ultralight-wing: controller position tracking performance for $\|P_x\|_2$, $\|P_y\|_2$, $\|P_z\|_2$.

TABLE V(A)
LONG-WING: MEAN MOTOR PWM COMMAND; % ACTUATION EFFORT REDUCED OVER NDI

Trajectory	INDI (Mean ± σ)	NDI (Mean ± σ)	Δ Mean (%) [2]
Circle	30 200 ± 700	31 600 ± 900	–4.4
Elevated circle	30 900 ± 800	32 400 ± 700	–4.6
Lemniscate	29 600 ± 700	32 300 ± 800	–8.4

TABLE V(B)
LONG-WING: MEAN BODY YAW ROTATIONAL RATE (HZ); % ROTATIONAL RATE REDUCED OVER NDI

Trajectory	INDI (Mean ± σ)	NDI (Mean ± σ)	Δ Mean (%) [2]
Circle	6.3 ± 0.1	6.1 ± 0.15	+3.2
Elevated circle	5.9 ± 0.1	6.2 ± 0.15	-4.8
Lemniscate	5.9 ± 0.1	6.1 ± 0.15	-3.2

TABLE VI
AGGREGATED ERRORS (MEAN ±σ, M) FROM FIGS. 13 AND 14 ACROSS ALL TRAJECTORIES; % ERROR REDUCED OVER ATT

SAM	Error	ATT	INDI (Δ%)	NDI (Δ%)
Long-wing	$\|P_x\|_2$	0.71 ± 0.08	0.27 ± 0.09 (–62)	0.30 ± 0.07 (–58)
	$\|P_y\|_2$	0.65 ± 0.03	0.23 ± 0.03 (–65)	0.25 ± 0.02 (–62)
	$\|P_z\|_2$	0.07 ± 0.01	0.06 ± 0.01 (–14)	0.07 ± 0.01 (0)
Short-wing	$\|P_x\|_2$	0.80 ± 0.02	0.54 ± 0.02 (–33)	0.61 ± 0.02 (–24)
	$\|P_y\|_2$	0.80 ± 0.13	0.48 ± 0.04 (–40)	0.51 ± 0.04 (–36)
	$\|P_z\|_2$	0.08 ± 0.01	0.08 ± 0.01 (0)	0.08 ± 0.01 (0)

2) Long-Wing, Short-Wing (INDI Vs. NDI Vs. ATT): As summarized in Table VI, INDI offers significantly improved position tracking over both NDI and baseline ATT across long- and short-wing configurations. On the long-wing, INDI reduces $\|Px\|_2$ and $\|Py\|_2$ by 62%[3] and 65%[3], respectively, compared to ATT, whilst NDI achieves a lower 58% and 62% in reductions, indicating that INDI consistently yields better horizontal control performance. Even for $\|Pz\|_2$, where all controllers performed well, INDI still improves upon ATT by 14%[3], while NDI shows no improvement. For the short-wing platform, INDI reduces $\|Px\|_2$ and $\|Py\|_2$ by 33%[3] and 40%[3] respectively, again outperforming NDI's 24% and 36% reductions. Both

[3]Higher %error reductions over ATT are colored in green in Table VI.

IEEE Robotics and Automation Letters (RA-L) paper, presented at ICRA 2026, Vienna, Austria. Cite as RA-L paper.

TABLE VII
ULTRALIGHT-WING: AGGREGATED ERRORS (MEAN $\pm\sigma$, M) FROM FIG. 15 ACROSS ALL TRAJECTORIES; % ERROR REDUCED OVER NDI

Error	INDI (Mean ± σ)	NDI (Mean ± σ)	Δ Mean (%) [1]
$\|P_x\|_2$	0.78 ± 0.18	0.82 ± 0.13	-4.9
$\|P_y\|_2$	0.80 ± 0.15	0.79 ± 0.10	+1.3
$\|P_z\|_2$	0.09 ± 0.01	0.09 ± 0.01	0.0

controllers perform equally in altitude tracking. These results reaffirm INDI's disturbance rejection capability in Section V-F1, which leads to more accurate and consistent trajectory tracking for both wings.

3) Ultralight-Wing (INDI Vs. NDI): As shown in Table VII, the ultralight-wing, with a third in thrust margin compared to the other wings (Table II), operates under significantly constrained actuation authority. This limits its achievable speed (reduced $\|\overline{\mathbf{V_{Ref}}}\|_2$ in Table III to 0.3 m/s) and trajectory complexity (circle and elevated circle only). Despite these hardware limitations, INDI exhibits superior or comparable tracking performance to NDI. Specifically, INDI reduces $\|P_x\|_2$ by 4.9% and matches vertical accuracy, while incurring a marginal +1.3% increase in $\|P_y\|_2$. These results further highlight INDI's robustness even with weaker and less responsive actuation.

VI. CONCLUSION

Through rigorous quantitative evaluation across three distinct wing morphologies and trajectory profiles, we demonstrate that INDI significantly outperforms NDI and purely attitude control in precision, efficiency, and robustness. Compared to NDI, INDI achieves substantial improvements in angular acceleration tracking (up to 13.8%), motor actuation efficiency (up to 8.4% lower PWM), and body rate stability, particularly in high-curvature or dynamically intense segments. To top it off, INDI secures up to 65% improvement (highest) in position tracking over ATT. Notably, INDI sustains these advantages even under the thrust-limited regime of the ultralight-wing, reinforcing its versatility and resilience. These results validate INDI as a control framework well-suited for severely under-actuated SAMs. For future work, there is strong consideration of utilizing onboard gyros from boards such as the Bolt to handle angular derivative tracking, of which wing designs can only operate well beneath the gyro saturation limit.

ACKNOWLEDGMENT

The authors would like to thank Chi Trinh for her help with photographing the static display and night flights, and Wei Jun Ang for his computer-aided design of the SAM in the relevant system modeling figures.

REFERENCES

[1] X. Cai, S. Zhong, T. M. Tan, W. J. Ang, and S. Foong, "Design and optimization of a samara-inspired lightweight monocopter for extended endurance," *IEEE Robot. Automat. Lett.*, vol. 10, no. 7, pp. 7214–7221, Jul. 2025.

[2] L. S. T. Win, S. K. H. Win, D. Sufiyan, G. S. Soh, and S. Foong, "Achieving efficient controlled flight with a single actuator," in *Proc. IEEE/ASME Int. Conf. Adv. Intell. Mechatron.*, 2020, pp. 1625–1631.

[3] X. Cai, S. K. H. Win, H. Bhardwaj, and S. Foong, "Modeling, control and implementation of adaptive reconfigurable ROtary wings (ARROWs)," *IEEE/ASME Trans. Mechatron.*, vol. 28, no. 4, pp. 2282–2292, Aug. 2023.

[4] E. Tal and S. Karaman, "Accurate tracking of aggressive quadrotor trajectories using incremental nonlinear dynamic inversion and differential flatness," *IEEE Trans. Control Syst. Technol.*, vol. 29, no. 3, pp. 1203–1218, May 2021.

[5] E. J. Smeur, G. C. de Croon, and Q. Chu, "Cascaded incremental nonlinear dynamic inversion for MAV disturbance rejection," *Control Eng. Pract.*, vol. 73, pp. 79–90, 2018.

[6] S. Sieberling, Q. P. Chu, and J. A. Mulder, "Robust flight control using incremental nonlinear dynamic inversion and angular acceleration prediction," *J. Guid., Control, Dyn.*, vol. 33, no. 6, pp. 1732–1742, 2010.

[7] P. Simplićio, M. D. Pavel, E. Van Kampen, and Q. P. Chu, "An acceleration measurements-based approach for helicopter nonlinear flight control using incremental nonlinear dynamic inversion," *Control Eng. Pract.*, vol. 21, no. 8, pp. 1065–1077, 2013.

[8] P. Smith, "A simplified approach to nonlinear dynamic inversion based flight control," in *Proc. 23rd Atmosph. Flight Mechan. Conf.*, 1998, pp. 4461–4469.

[9] B. P. Acquatella and Q. P. Chu, "Agile spacecraft attitude control: An incremental nonlinear dynamic inversion approach," *IFAC-PapersOnLine*, vol. 53, no. 2, pp. 5709–5716, 2020.

[10] J. Hauser, S. Sastry, and G. Meyer, "Nonlinear control design for slightly non-minimum phase systems: Application to V/STOL aircraft," *Automatica*, vol. 28, no. 4, pp. 665–679, 1992.

[11] J.-J. E. Slotine et al., *Applied Nonlinear Control*, vol. 199. Englewood Cliffs, NJ, USA: Prentice-Hall, 1991.

[12] S. Sun, A. Romero, P. Foehn, E. Kaufmann, and D. Scaramuzza, "A comparative study of nonlinear MPC and differential-flatness-based control for quadrotor agile flight," *IEEE Trans. Robot.*, vol. 38, no. 6, pp. 3357–3373, Dec. 2022.

[13] R. Coelho, A. Moutinho, and J. R. Azinheira, "Quadrotor attitude control using incremental nonlinear dynamics inversion," in *Proc. Int. Conf. Inform. Control, Automat. Robot.*, 2017, pp. 98–109.

[14] D. Lee, H. Jin Kim, and S. Sastry, "Feedback linearization vs. adaptive sliding mode control for a quadrotor helicopter," *Int. J. Control, Automat. Syst.*, vol. 7, pp. 419–428, 2009.

[15] A. Kellas, "The guided samara: Design and development of a controllable single-bladed autorotating vehicle," Ph.D. thesis, Massachusetts Institute of Technology, Cambridge, MA, USA, 2007.

[16] J. Houghton and W. Hoburg, "Fly-by-wire control of a monocopter," Massachusetts Institute of Technology, Cambridge, MA, USA, Project Report, 16.622, 2008.

[17] S. K. H. Win, L. S. T. Win, D. Sufiyan, and S. Foong, "Design and control of the first foldable single-actuator rotary wing micro aerial vehicle," *Bioinspiration Biomimetics*, vol. 16, no. 6, 2021, Art. no. 66019.

[18] E. Tang, W. J. Ang, K. W. Tan, and S. Foong, "Harnessing the differential flatness of monocopter dynamics for the purpose of trajectory tracking in a stable invertible coaxial actuated ROtorcraft (SICARO)," in *Proc. 2024 IEEE Int. Conf. Robot. Automat.*, 2024, pp. 6145–6151.

[19] J. Levine, *Analysis and Control of Nonlinear Systems: A Flatness-Based Approach*. Berlin, Germany: Springer, 2009.

[20] E. Tang, W. J. Ang, K. Wee Tan, and S. Foong, "Design and control of a stable invertible coaxial actuated ROtorcraft (SICARO)," in *Proc. IEEE/ASME Int. Conf. Adv. Intell. Mechatron.*, 2023, pp. 255–262.

[21] G. J. Leishman, *Princ. of Helicopter Aerodynamics With CD Extra*. New York, NY, USA: Cambridge Univ. Press, 2006.

[22] M. Faessler, A. Franchi, and D. Scaramuzza, "Differential flatness of quadrotor dynamics subject to rotor drag for accurate tracking of high-speed trajectories," *IEEE Robot. Automat. Lett.*, vol. 3, no. 2, pp. 620–626, Apr. 2018.

[23] D. Brescianini, M. Hehn, and R. D'Andrea, "Nonlinear quadrocopter attitude control: Technical report," ETH Zürich, Zürich, Switzerland, Tech. Rep., 2013.

[24] J. Diebel et al., "Representing attitude: Euler angles, unit quaternions, and rotation vectors," *Matrix*, vol. 58, no. 15/16, pp. 1–35, 2006.

[25] Bitcraze, "Crazyflie bolt 1.1 - product specification," Online, 2020, Accessed: Apr. 28, 2025. [Online]. Available: https://www.bitcraze.io/products/crazyflie-bolt-1-1/

[26] K. Youcef-Toumi and S.-T. Wu, "Input/output linearization using time delay control," *J. Dyn. Syst., Meas., Control*, vol. 114, no. 1, pp. 10–19, 1992. doi: 10.1115/1.2896491.